Lab on a Chip

PAPER

View Article Online
View Journal | View Issue

Cite this: *Lab Chip*, 2021, **21**, 1096

A fully transparent, flexible PEDOT:PSS–ITO–Ag–ITO based microelectrode array for ECoG recording†

Weiyang Yang, *[a] Yan Gong,[a] Cheng-You Yao,[a] Maheshwar Shrestha,[b] Yaoyao Jia,[c] Zhen Qiu,[a] Qi Hua Fan,[b] Arthur Weber[d] and Wen Li[a]

Integrative neural interfaces combining neurophysiology and optogenetics with neural imaging provide numerous opportunities for neuroscientists to study the structure and function of neural circuits in the brain. Such a comprehensive interface demands miniature electrode arrays with high transparency, mechanical flexibility, electrical conductivity, and biocompatibility. Conventional transparent microelectrodes made of a single material, such as indium tin oxide (ITO), ultrathin metals, graphene and poly-(3,4-ethylenedioxythiophene)/poly(styrenesulfonate) (PEDOT:PSS), hardly possess the desired combination of those properties. Herein, ultra-flexible, highly conductive and fully transparent microscale electrocorticogram (μECoG) electrode arrays made of a PEDOT:PSS–ITO–Ag–ITO assembly are constructed on thin parylene C films. The PEDOT:PSS–ITO–Ag–ITO assembly achieves a maximum ~14% enhancement in light transmission over a broad spectrum (350–650 nm), a significant reduction in electrochemical impedance by 91.25%, and an increase in charge storage capacitance by 1229.78 μC cm^{-2}. Peeling, bending, and Young's modulus tests verify the enhanced mechanical flexibility and robustness of the multilayer assembly. The μECoG electrodes enable electrical recordings with high signal-to-noise ratios (SNRs) (~35–36 dB) under different color photostimulations, suggesting that the electrodes are resilient to photon-induced artifacts. *In vivo* animal experiments confirm that our array can successfully record light-evoked ECoG oscillations from the primary visual cortex (V1) of an anesthetized rat.

Received 5th November 2020,
Accepted 21st January 2021

DOI: 10.1039/d0lc01123a

rsc.li/loc

Introduction

Neurological disorders and diseases in central and peripheral nervous systems, such as Parkinson's disease, Alzheimer's disease, epilepsy, *etc.*, affect hundreds of millions of people worldwide.[1] Besides commercially-available medications and deep brain stimulation approaches,[2,3] numerous neural interface electrodes have been developed to allow researchers to stimulate and record neural activity with high temporal resolution,[4] permitting quantitative studies of the correlation between neural function and dysfunction. However, most existing microelectrode techniques cannot achieve cell-type specific neuromodulation and high spatial resolution due to current spread in tissues.

Optogenetics, a technique that uses light to control genetically targeted neurons,[5,6] has emerged as a viable alternative that overcomes the limitations associated with microelectrode technologies.[7,8] However, optical imaging methods have not achieved the high temporal resolution seen with microelectrodes. Leveraging the advantages of both technologies, hybrid optoelectronic neural interface tools that combine optogenetic neurostimulators with microscale electrocorticogram (μECoG) recording electrodes have been proposed by several groups.[9,10] Although most of the existing ECoG arrays are used to only gather the electrophysiological signals from the superficial surface of the cerebral cortex, some ECoG arrays with high spatial resolution, such as 'NeuroGrid', have been proved to be capable of recording spike activity and LFPs.[11] In such devices, transparent μECoG electrodes allow more light to penetrate through the electrode array, and therefore are more beneficial than their opaque counterparts.

To date, most transparent μECoG arrays are fabricated with a single material, including indium tin oxide (ITO), ultrathin metals, micro/nanostructured metals, graphene and poly-(3,4-ethylenedioxythiophene)/poly(styrenesulfonate) (PEDOT:PSS). However, utilizing only a single material is

[a] *The Institute for Quantitative Health Science & Engineering, Michigan State University, 775 Woodlot Dr, East Lansing, MI, 48824, USA. E-mail: yangweiy@msu.edu*
[b] *Engineering Research Complex, Michigan State University, 1497 Engineering Research Ct, East Lansing, MI, 48824, USA*
[c] *North Carolina State University, Engineering Bldg II, Raleigh, NC, 27606, USA*
[d] *Biomedical Physical Sciences, Michigan State University, 567 Wilson Rd, East Lansing, MI, 48823, USA*

† Electronic supplementary information (ESI) available: Fig. S1–S8. See DOI: 10.1039/d0lc01123a

hard to achieve the desired combination of excellent electrical, optical, mechanical, and biocompatible properties.

For example, ITO is most commonly used because of its relatively high transmittance over the entire visible spectrum,[12] biocompatibility,[13] and good electrical conductivity.[12] However, the mechanical flexibility of ITO remains a challenge due to its high Young's modulus,[14] especially when relatively thick ITO (100 nm) is required for performing both good transmittance and conductivity. Besides, ITO microelectrodes face a critical problem of the high electrochemical impedance, which would lead to undesirable electrochemical reactions with the brain tissue.[15]

Ultrathin metals enable higher conductivity (in the range of ohms) than ITO but cannot achieve high transparency and conductivity simultaneously due to their limited optical transmittance of ~50–70% even with ~4–12 nm thickness.[16] Therefore, micro/nanostructured metals, such as nanomesh or microgrid, have been proposed as an alternative, which enables improved transmittance compared to ultrathin metal films.[17,18] For example, Seo *et al.* report Au nanomesh electrodes with over 70% transmittance at 550 nm, good flexibility, low sheet resistance of 0.9–18 Ω sq^{-1} and electrochemical impedance of 8.14 Ω cm^2.[17] Electrodepositing PEDOT:PSS on top of Au nanomesh to make bilayer nanomesh further improves the electrical properties.[19–21] Despite its many benefits, the Au nanomesh significantly reduces the effective recording area because of the large hollow structures on the electrode.

Most recently, graphene has emerged as a promising material for making transparent electrodes on account of its broadband transparency, good conductivity, biocompatibility and flexibility.[22–24] However, it is hard to grow high-quality, large-scale graphene on the polymer substrates because either high temperatures (>1000 °C) or specific substrate materials are required. To address these challenges, engineering methods have been explored to transfer graphene from rigid substrates to flexible polymer substrates.[22] However, those methods are laborious and tedious and reduce the yield and reproducibility.

As an attractive conductive polymer, PEDOT:PSS excels in the fabrication of microelectrodes for neural interface applications, owing to its outstanding biocompatibility, excellent stability, transparency, and flexibility.[25] However, compared to other transparent conducting materials, the relatively low electrical conductivity of PEDOT:PSS makes it unsuitable for use in high-density electrode arrays.

Therefore, we report, for the first time, a conductive, ultra-flexible, anti-reflective and transparent μECoG array utilizing a multilayer PEDOT:PSS–ITO–Ag–ITO thin film structure on parylene C. Combining thin film materials of different refractive indices, we can selectively tune and optimize the optical reflectivity and transmissivity of the multilayer stack at specific wavelengths while maintaining its superior mechanical flexibility and stability. A well-designed multilayer stack also can take advantage of dominant materials to enhance its electrical conductivity. We chose three transparent thin-film materials as the building blocks of the stack assembly: silver (Ag), PEDOT:PSS, ITO. Thin-film Ag (~10 nm) is highly conductive, mechanically flexible, and optically transparent over a spectrum of 150 nm.[26] ITO offers excellent transparency while being chemically stable and biocompatible to protect Ag from corrosive biological environments. PEDOT:PSS serves to further reduce electrochemical impedance as well as enhance optical transmittance and flexibility. To design the PEDOT:PSS–ITO–Ag–ITO stack, an admittance loci thin-film design method was used to calculate the optimal thickness of each layer with the lowest theoretical reflectance under the preferred wavelengths of 470 nm, 550 nm, and 630 nm. The best thickness combination was based on empirical results and material property requirements.[27] We then studied in detail the transparency, conductivity, electrochemical performance, mechanical properties, and stability of the combined PEDOT:PSS–ITO–Ag–ITO film optimized for 550 nm.

Results and discussion

Temperature dependence of sputter ITO performance

ITO must be deposited at temperatures lower than 80–100 °C, the range of the glass transition temperature of parylene C to avoid polymer degradation. Therefore, the influence of the processing temperature on the performance of ITO thin films was studied to lay the basis for further development of the multilayer assembly. For these experiments, ITO films with a common thickness of 100 nm were sputtered on either glass or parylene-coated glass substrates at selected temperatures of 22 °C, 69 °C, 92 °C, 116 °C and 140 °C. Fig. 1a and b show the average transmittances (n = 5) of ITO films deposited on different substrates. The ITO-on-glass samples show no significant changes in the film transmittance within a wavelength range of 300–800 nm when the sputtering temperature was lower than 92 °C. As the temperature increased over 116 °C, the wavelength of the peak transmittance gradually shifted down from 441 nm to 386 nm. At 140 °C, the peak transmittance increased by 2.186%, mainly due to ITO crystallization at high sputtering temperatures. The optical transparency of the ITO-on-parylene films exhibited an inverse trend in temperature dependence. While the peak wavelength shifted forward slightly from 493 nm to 450 nm as the sputtering temperature increased, the peak transmittance decreased from ~85% to ~78%. This reduction in transmittance could be mainly caused by oxidation degradation of parylene C aromatic rings in air at temperatures greater than its glass transition temperature, which produces accumulated carboxylic acids in polymer chains, resulting in discoloration, cracks, and brittleness of the film. The periodic waves in Fig. 1b are due to the light interference. The resistivity decreased from 6.1×10^{-4} Ω cm to 2.4×10^{-4} Ω cm for ITO on glass and from 6.2×10^{-4} Ω cm to 3.3×10^{-4} Ω cm for ITO on parylene C, as shown in Fig. 1c. The resistivity of our room-temperature sputter ITO (6.1×10^{-4} Ω cm) is close to

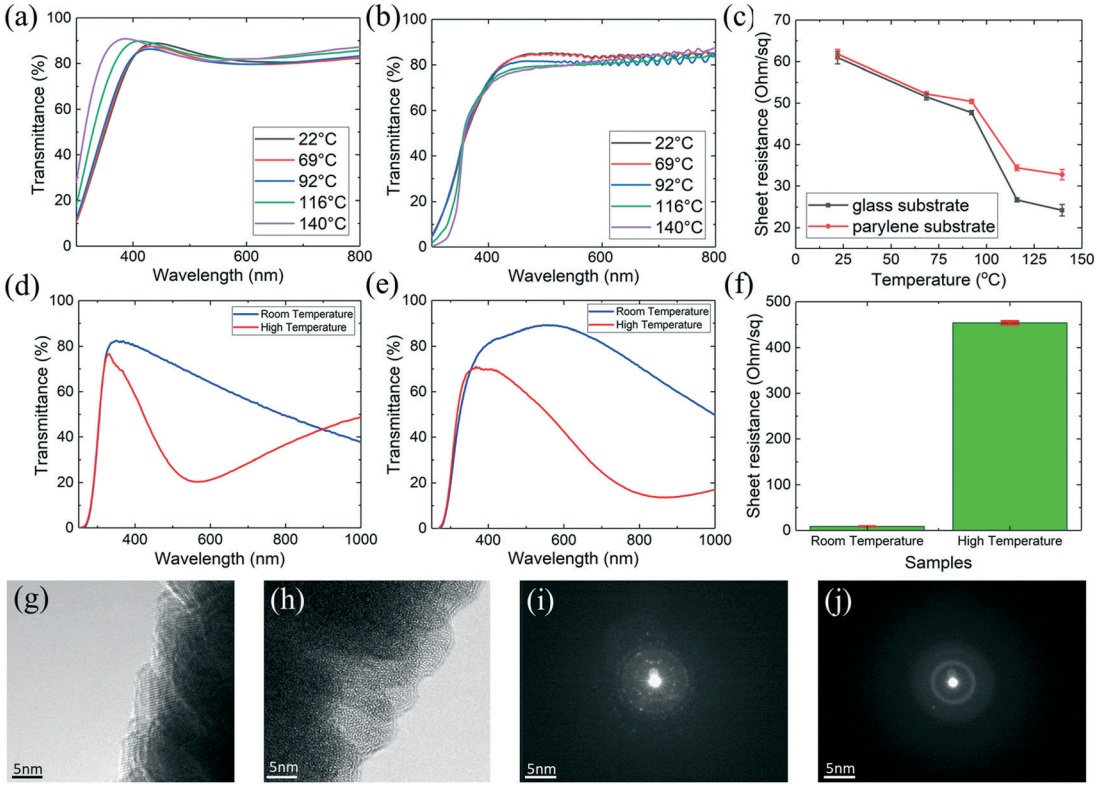

Fig. 1 Temperature dependence of optical and electrical properties of sputtered ITO and Ag thin films. Transmittances of 100 nm ITO deposited under sputtering temperatures of 22 °C, 69 °C, 92 °C, 116 °C, and 140 °C on a glass slides and b parylene C coated glass slides. c Sheet resistances of 100 nm ITO deposited under different sputtering temperatures on glass slides and parylene C coated glass slides, respectively. Transmittances of d Ag (9.45 nm) and e ITO (24 nm)–Ag (9.45 nm)–ITO (20 nm) deposited under the sputtering temperature of room temperature and high temperature (116 °C) on glass slides. f Sheet resistances of ITO (24 nm)–Ag (9.5 nm)–ITO (20 nm) at room temperature and high temperature (116 °C) on glass slides, respectively. High-resolution TEM images of g polycrystalline structure of high-temperature ITO, h amorphous structure of room-temperature ITO. X-ray diffraction patterns of i high-temperature ITO and j room-temperature ITO.

that of excimer laser annealed ITO (2.5×10^{-4} Ω cm)[28] and better than that of low-temperature plasma annealed ITO (2.5×10^{-3} Ω cm)[29] as reported in the literature.

The crystallization of the ITO films sputtered at room temperature and 110 °C was analyzed using transmission electron microscopy (TEM), as shown in Fig. 1g–j. The room temperature deposited ITO films were mostly amorphous (Fig. 1h) with some degree of crystallites in small areas. When the sputtering temperature increased, the amorphous ITO films were crystallized and densified as demonstrated in Fig. 1g and i. The crystallization of thin ITO films can significantly improve the film quality, resulting in better optical transparency and electrical conductivity. This is consistent with our results obtained from the ITO-on-glass samples and the findings of other groups.[30]

Despite the good performance of the high-temperature ITO films, the overall conductance of the PEDOT:PSS–ITO–Ag–ITO assembly is a result of the parallel combination of the four individual layers (Fig. 2b and S1†), and is dominated by the Ag layer which has the lowest sheet resistivity (1.59×10^{-6} Ω cm) among these three materials.[31] Hence, the improved conductivity of high-temperature ITO does not play a significant role. As ITO and Ag were deposited consecutively in the same sputtering system, high-temperature processing may also deteriorate the quality of Ag thin films due to oxidation (Fig. 1d–f), therefore causing decreased transmittance over 400 nm wavelength. Moreover, as shown in Fig. 1b, the combined ITO–parylene C film exhibits higher transmittance between ~400 nm and ~600 nm at lower sputtering temperatures. Having considered the tradeoffs between the ITO quality and the overall performance of the assembly, we chose room-temperature sputtered ITO as the electrode material for the following experiments.

PEDOT:PSS–ITO–Ag–ITO on parylene assembly

Fig. 2a and b shows the concept diagram of μECoG array with PEDOT:PSS–ITO–Ag–ITO on parylene C assembly. The thickness of each individual layer was simulated using an equivalent admittance method (Fig. S2†)[32,33] to minimize the reflectance at inhomogeneous thin film interfaces and maximize the admittance of the combined film at the desired wavelength. Fig. 2c and d show an example of PEDOT:PSS (30.5 nm)–ITO (24 nm)–Ag (9.45 nm)–ITO (20 nm) assemblies with peak transmittance optimized at 550 nm. Compared with single-layer ITO of equivalent thickness, the assembly

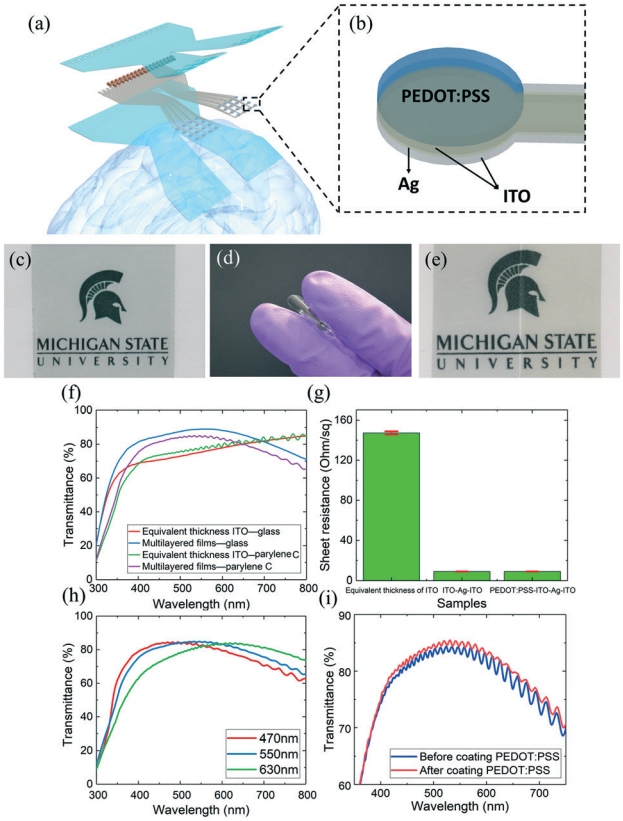

Fig. 2 a Concept diagram of transparent μECoG array. b Concept diagram of PEDOT:PSS–ITO–Ag–ITO on parylene C. c Excellent transparency and d flexibility of multilayered thin films. e The transparency before (right) and after (left) PEDOT:PSS coating. f Transmittances of the combined films compared with the equivalent thickness ITO on the glass and parylene C substrate, respectively. g Average sheet resistances (n = 5) of PEDOT:PSS–ITO–Ag–ITO and the equivalent thickness of ITO on the parylene C substrate. h The tunable peak transmittances of combined PEDOT:PSS–ITO–Ag–ITO films on parylene C at wavelengths of 470 nm, 550 nm, and 630 nm, respectively. i The transmittance before (right) and after (left) adding the PEDOT:PSS coating.

had a significant increase in transmittance throughout the visible spectrum from 350 nm to 700 nm on both parylene C and glass substrates. The peak transmittance at 550 nm was enhanced by ~7% from ~78% to ~85% on parylene C, and by ~14% from ~75% to ~89% on glass (Fig. 2f). The four-point probe measurements were performed on five different regions over the entire substrate, confirming that the average sheet resist was significantly reduced from 147.5 ± 1.53 Ω sq^{-1} (1.24×10^{-3} Ω cm resistivity) to 8.81 ± 0 Ω sq^{-1} (7.40×10^{-5} Ω cm resistivity) for the combined film, as shown in Fig. 2g. There was no change in the sheet resistance before and after adding PEDOT:PSS to the ITO–Ag–ITO stack. Fig. 2h proves that the peak transmittance of the combined film can be tuned to preferred wavelengths, such as 470 nm, 550 nm, and 630 nm, using the admittance loci simulation. This is an important quality for many optical applications, especially optogenetics that utilizes different wavelength light to activate (470 nm for channelrhodopsin) or inhibit (535 nm for halorhodopsin) the activity of light-sensitive ion channel proteins.[34] Fig. 2i shows that the additional coating of 30 nm PEDOT:PSS on ITO–Ag–ITO resulted in ~2% improvement in peak transmittance at 550 nm since the PEDOT:PSS coating acted as an anti-reflective layer. Fig. 2e shows that the color of the thin films changed from light yellow (right) to light blue (left) after spin-coating PEDOT:PSS. There was a neglectable change in the film's sheet resistance before and after adding PEDOT:PSS, due to the higher resistivity of PEDOT:PSS over Ag.

Fig. 3a and b show the Bode plots of the electrochemical impedance magnitudes and phases of the ITO, ITO–Ag–ITO, and PEDOT:PSS–ITO–Ag–ITO *versus* frequency, respectively. The ITO–Ag–ITO structure effectively reduced the film impedance over a wide frequency range (0.1 Hz–100 kHz), while the PEDOT:PSS coating further decreased the electrochemical impedance, consistent with previous results in the literature.[11] The 1 kHz electrochemical impedance of the total combined film decreased by over an order of magnitude, from 322.49 Ω cm^2 to 26.29 Ω cm^2 for the pure ITO film. Fig. 3c plots the cyclic voltammetry (CV) scans of both the single-layer ITO and multilayer PEDOT:PSS–ITO–Ag–ITO–parylene films. The charge density (C_p) of the films was calculated from the CV curves using eqn (1)

$$C_p = \frac{A}{2ak(V_2 - V_1)} \quad (1)$$

where A is the area inside the CV curve, a is the area of working electrode, k is the scan rate of CV in V s^{-1}, and (V_2 – V_1) is the potential window. Charge density is often used to determine the charge-storage capacity (CSC) of microelectrodes (CSC = $a \times C_p$), which is an important predictor of how much charge an electrode can inject during neurostimulation. Our results show that the combined film has a charge density of 1259.65 μC cm^{-2}, over 40 times larger than that of the single-layer ITO film (29.87 μC cm^{-2}).

The improvement in impedance and charge storage capacity can be attributed mainly to the increased surface roughness of the PEDOT:PSS coating (Fig. S3†).[11] The rough surface provides a larger electroactive area of the electrode when exposed to the electrolyte, allowing an increase of charge injection per unit area at the electrode–electrolyte interface. This result is consistent with our previous findings and those in literature.[11] Moreover, the interchain interaction between PEDOT and PSS results in conformational changes for the PEDOT chains from a coil to linear structure, which also increases the solid-state conductivity of PEDOT.[35] The reduced impedance and the increased charge storage capacity both contribute to the decrease of the total impedance at the electrode–electrolyte interface, therefore, enabling electrophysiology recording with high signal to noise ratio (SNR).

To evaluate the stability of the combined thin films, first, we repeated the CV scan of the same sample at room in the saline solution for 10 consecutive cycles. No significant changes in CV curves were observed among 10 cycles, as

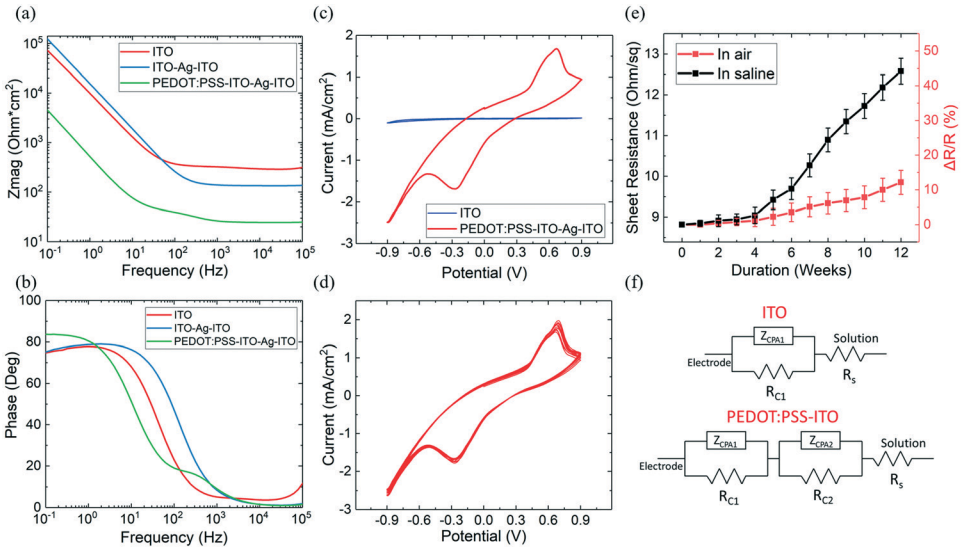

Fig. 3 Electrochemical impedance and cyclic voltammetry of PEDOT:PSS–ITO–Ag–ITO thin films. a Electrochemical impedance magnitudes and b phases of the plain ITO, ITO–Ag–ITO, and PEDOT:PSS–ITO–Ag–ITO *versus* the frequency, respectively. c CVs of the plain ITO and PEDOT:PSS–ITO–Ag–ITO WEs *versus* Ag/AgCl RE, showing that the PEDOT:PSS–ITO–Ag–ITO electrode exhibits larger charge storage capacity. d CVs of the PEDOT:PSS–ITO–Ag–ITO electrode for 10 cycles, demonstrating the stability of the multilayered structures in saline. e Sheet resistance changes (n = 5) of the combined films in air and in saline at 37 °C. f Equivalent circuit models of the pure ITO and the ITO–PEDOT:PSS electrode–electrolyte interface.

shown in Fig. 3d. Then we assessed the long-term stability of combined films using accelerated testing at 37 °C in air and saline environments, respectively. As shown in Fig. 3e, the combined films exhibited excellent stability with only a slight resistance increase of less than 1.25% and 2.75% after four-week exposure in air and saline, respectively. At the 12 week endpoint, the combined films tested in air still exhibited good stability with an overall resistance increase of less than 12.14%, while the samples tested in saline had a resistance increase of ~44.18%. The increase in sheet resistance may be due to the reaction of Ag with oxygen and moisture. Moisture can also weaken the bonding strength at the interfaces between multilayer thin films, which will lead to delamination, and thus, accelerated degradation of the film quality. Nevertheless, because the initial sheet resistance of our combined films was only 8.81 Ω sq^{-1}, the 44.18% increase in sheet resistance to 12.70 Ω sq^{-1} was still acceptable for the intended applications in the neural recording.

Fig. 3f shows the equivalent circuit models of the films before and after adding PEDOT:PSS as discussed in our recent study.[11] Compared to the single-layer ITO film, the combined film contained additional Z_{CPA}–R_C circuit elements in parallel with the initial Z_{CPA}–R_C. The first Z_{CPA}–R_C parallel element represents the electron transfer occurring at the ITO–PEDOT:PSS interface while the second Z_{CPA}–R_C element represents the charge transfer reaction at the PEDOT:PSS–electrolyte interface. The two parallel elements were put in series with the solution resistance R_S. Based on this model, the fitted R_C exhibit a decrease by 6 orders of magnitude at both the ITO–PEDOT:PSS and PEDOT:PSS-solution interfaces.[11] Meanwhile, the PEDOT:PSS–electrolyte interface shows a lower Z_{CPA} value by 6 orders than the ITO–electrolyte interface. As such, the total impedance magnitude of ITO–PEDOT:PSS was much smaller than that of the single-layer ITO film.[11]

Peeling tests were performed on five samples to evaluate the bonding strength of the room temperature sputtered ITO on the parylene C substrate without any adhesion promoting layer.[36] The tested sample area was inspected visually after 0, 1, 10, and 50 times of peel-off, as given in Fig. 4a–c and S4.† We did not observe any ITO delamination from parylene C in all samples, indicating strong bonding between the room-temperature ITO coating and the parylene substrate. Except samples 1 and 2, for samples 3, 4 and 5, 8%, 33% and 53% of parylene C delamination were detected during 50 cycles of peeling tests, as shown in Table 1. This is mainly due to the poor adhesion between parylene C and glass.

Bending tests were performed to validate the flexibility of the combined films with different ITO thicknesses. Three film combinations proceeded to tensile bending, including 37 nm ITO–10 nm Ag–33 nm ITO, 15 nm ITO–10 nm Ag–38.5 nm ITO, and 20 nm ITO–9.5 nm Ag–24 nm ITO, and their testing results were compared to single-layer ITO films with the equivalent thicknesses of 70 nm, 53.5 nm, and 44 nm, respectively. The changes in the sheet resistance were measured and then normalized as $\Delta R/R$, where R was the initially measured sheet resistance and ΔR was the difference in the sheet resistance before and after bending cycles. Bending curvatures with diameters of 3 mm and 6 mm were tested individually to study how the sheet resistance changed with different degrees of bending. As shown in Fig. 4d and e, for single-layer ITO, the films with thinner ITO are more robust to withstand bending. When combining thin ITO in

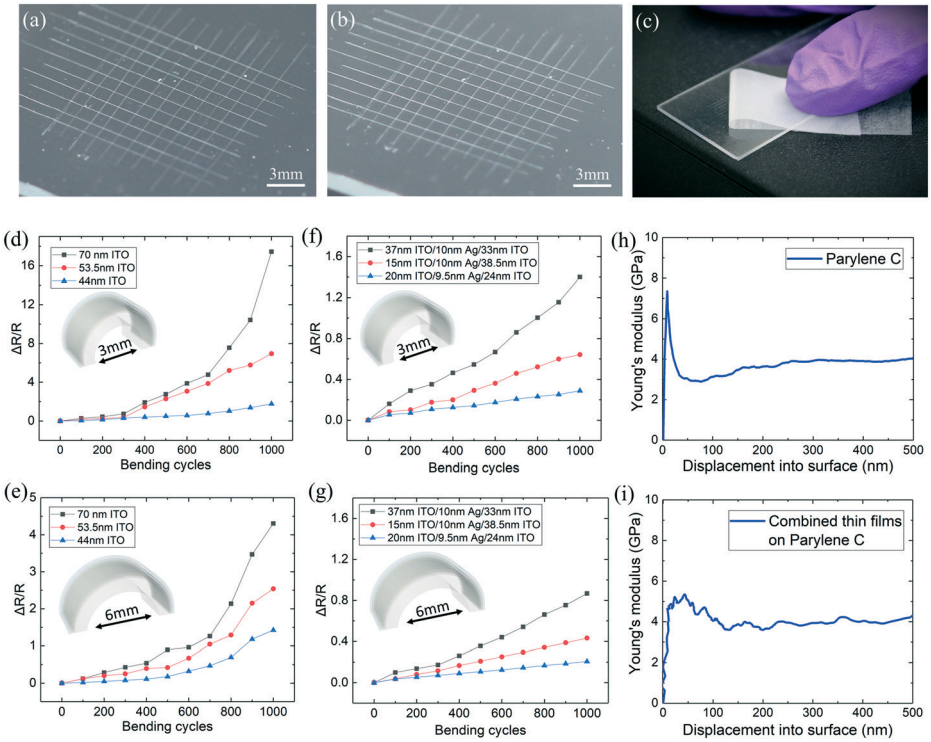

Fig. 4 Peel-off test results for evaluating the adhesion between ITO and parylene C interface on the glass slides and bending tests of the ITO–Ag–ITO multilayered assemblies and Young's modulus of the PEDOT:PSS–ITO–Ag–ITO on parylene C thin films. Photos of 100 1 × 1 mm^2 blade-scratched squares with a no peel-off, b 50 peel-off tests, c the peeling-off method. Sheet resistances of the combined thin films and single-layer ITO with the same total ITO thicknesses in 1000 bending cycles under d and f 3 mm and e and g 6 mm bending diameters, respectively. The Young's modulus of h the parylene C film and i the combined films.

the multilayer assembly shown in Fig. 4f and g, the films with the same thickness show significantly improved flexibility and tolerance to bending cycles. The results also indicated that, for a smaller bending diameter, the changes of sheet resistance were more noticeable but still within a good tolerance range of less than 140%.

Furthermore, we conducted cyclic nanoindentation tests to quantify Young's modulus of the parylene C films with and without the PEDOT:PSS–ITO–Ag–ITO coating. 36 indents were made on each sample, and Young's moduli of different samples were plotted in Fig. 4h and i as a function of the load displacement into the surface. The pointed shapes in the curves were corresponding to the pop-in events.[37] The Young's modulus after the first pop-in remained nearly constant at 4.049 GPa for parylene C and 4.064 GPa for the combined film after averaging all 36 indents. This result indicates that the added PEDOT:PSS–ITO–Ag–ITO coating has minimal impact on the overall Young's modulus of the combined film that is predominated by the polymer substrate. The small fluctuations in Fig. 4h were due to environment interference while the fluctuations in Fig. 4i were possibly associated with dislocation activities.[38] The experimental data were compared with theoretical calculations based on eqn (2) for less mixture of particle and polymer:

$$\frac{1}{E_{\text{composite}}} = \frac{V_{\text{ITO}_1}}{E_{\text{ITO}_1}} + \frac{V_{\text{Ag}}}{E_{\text{Ag}}} + \frac{V_{\text{ITO}_2}}{E_{\text{ITO}_2}} + \frac{V_{\text{Parylene}}}{E_{\text{Parylene}}} \quad (2)$$

where E is the Young's modulus and V is the volume fraction of each layer. With an assumption of the same cross-sectional area, the volume fraction was replaced by the layer thickness during the calculations. The Young's moduli of parylene C, ITO, and Ag are 4 GPa,[39] 116 GPa,[40] and 85 GPa, and the thicknesses were 10 μm, 44 nm, and 9.5 nm, respectively. The calculated $E_{\text{composite}}$ is 4.021 GPa, very close to the measured Young's moduli.

Table 1 Peeling test results with 5 samples

Samples	ITO delamination	Parylene C delamination
Sample 1	0%	0%
Sample 2	0%	0%
Sample 3	0%	8%
Sample 4	0%	33%
Sample 5	0%	53%

Microscale ECoG microelectrode arrays

Having characterized the performance of the combined films, a 32-channel μECoG array was designed and fabricated using the multilayer PEDOT:PSS–ITO–Ag–ITO film. The μECoG electrode array had dimensions of 16 mm × 10 mm, with two

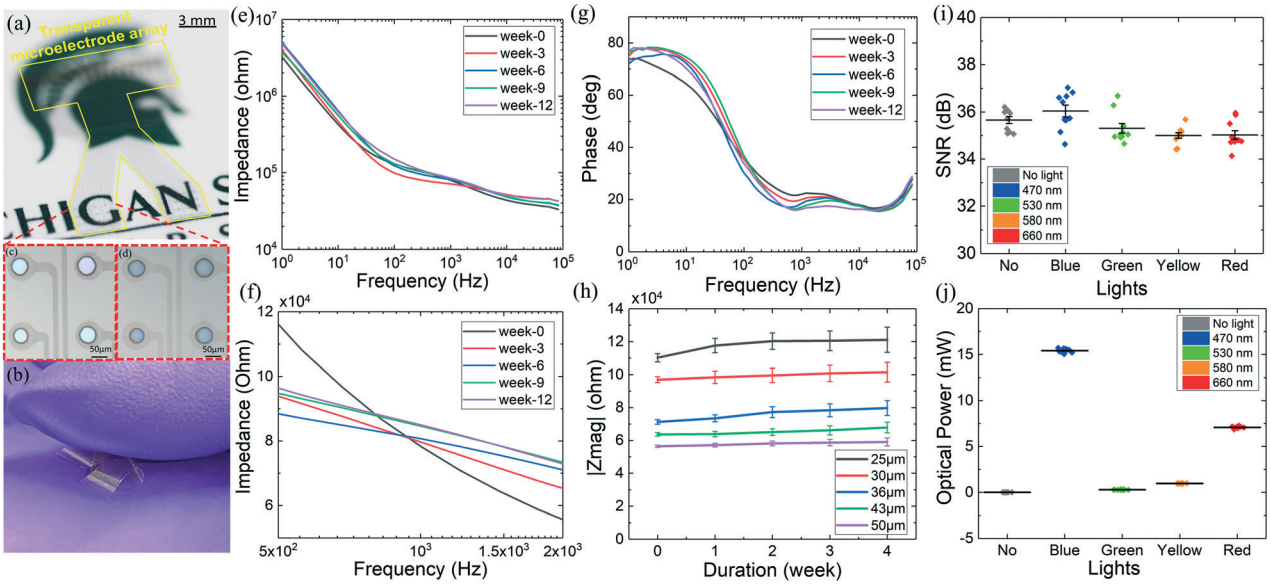

Fig. 5 The prototype of fabricated transparent and flexible μECoG microelectrodes arrays and their electrochemical impedance and SNR behaviours. a The transparency and b the flexibility of an as-fabricated μECoG microelectrode array without c and with d PEDOT:PSS coating. Impedance magnitude e and phase changes g of the PEDOT:PSS–ITO–Ag–ITO multilayered μECoG microelectrodes during 4 weeks soaking in room temperature saline. f Zoom-in impedance magnitudes at 1 kHz frequency over 4 weeks. h Average 1 kHz impedance changes of PEDOT:PSS–ITO–Ag–ITO microelectrodes, measured after being soaked in saline for 0 week, 1 week, 2 weeks, 3 weeks, and 4 weeks (n = 10). i SNRs of the μECoG microelectrode array (n = 10) under no light, ~470 nm blue, ~530 nm green, ~580 nm yellow, and ~660 nm red light illumination, respectively. j Optical powers of the blue LED (V = 3.3 V), green LED (V = 3.3 V), yellow LED (V = 1.8 V), and red LED (V = 1.8 V), respectively (n = 10).

3 mm × 3 mm panels to cover both left and right hemispheres of the primary visual cortex (V1) of the rat's brain. Each panel consisted of 16 microelectrodes with different diameters: 25 μm, 30 μm, 36 μm, 43 μm and 50 μm. Fig. 5a gives an example of the fabricated μECoG array, Fig. 5b and c show the ITO–Ag–ITO microelectrodes before and after the PEDOT:PSS treatment, and Fig. 5d demonstrates the flexibility of the array. Compared to the inkjet-printed PEDOT:PSS electrode with the electrochemical impedance of 12.675 Ω cm^2 at 1 kHz, our PEDOT:PSS treated electrode shows 4 times lower impedance of 3.257 Ω cm^2.[41] Recently reported electroplated PEDOT:PSS–graphene electrode indicated lower electrochemical impedance of under 0.21–0.3 Ω cm^2.[42,43] However, like most electroplated PEDOT:PSS, the PEDOT:PSS-coated electrode areas have low transparency or are not transparent.[42,43]

The stability of the μECoG electrode array was evaluated in air at room temperature for up to 12 weeks, during which impedance changes were monitored every three weeks and plotted in Fig. 5e–h. The zoom-in results in Fig. 5f show that the μECoG electrode array exhibited good stability over 12 weeks with an overall impedance increase of less than 8.47%. The average 1 kHz impedance decreased when the electrode area increased (Fig. 5h). The average 1 kHz impedance changes were less than 11.8% over 12 weeks for all the electrode diameters. This impedance increase may be due to PEDOT:PSS reaction with oxygen upon exposure to air, creating an aqueous acid environment that corrodes ITO.[44] ITO etching chemical will then diffuse through the PEDOT:PSS film and weaken the stability of the ITO–PEDOT:PSS interface, thereby slowly increasing impedance. Another possible reason for the increased impedance could be the corrosion reaction between Ag and the ionic solution that diffused through defects or pinholes in the top-most ITO layer.[45]

Increased noise and artifacts from the photoelectrochemical (PEC) effect, also known as the Becquerel effect, is a long-standing challenge for recording light-evoked neural activities in optogenetics. Therefore, we studied the effect of photon-induced artifacts on recording performance of the transparent μECoG electrode array. Fig. 5i shows the SNRs of recordings, measured from the μECoG microelectrodes (n = 10) in saline under room light as well as blue, green, yellow and red LED light. For all the light conditions, the average SNRs ranged from ~35 dB to ~36 dB with variations of less than 2.7%, indicating that the PEDOT:PSS–ITO–Ag–ITO electrodes are quite resistant to photoelectrochemical artifacts. The maximum forward LED voltages applied to different color LEDs were adjusted to achieve consistent illumination. Fig. 5j shows the corresponding optical powers of individual LEDs with forward voltages of V_{blue} = 3.3 V, V_{green} = 3.3 V, V_{yellow} = 1.8 V, and V_{red} = 1.8 V, respectively, measured in the solution at a distance of 0.5 cm from the LEDs. The blue LED had the strongest optical power of 16.2 mW among all the LEDs at the high applied voltage of 3.3 V. Although the same high 3.3 V voltage was applied on the green LED, the theoretical luminous efficacy of the green LED is much lower than the blue one. While preliminary, these results prove that optical stimulation with various light intensity and wavelengths

would have minimal impact on the recording quality of our μECoG microelectrodes.

To further evaluate the transmittance of the transparent microelectrodes of the μECoG array, we placed the μECoG array on a 50 μm-thick, mCherry-labelled, rat brain section. We inspected both the fluorescent and bright-field images from the same region of the brain section with and without the electrode array in place, as shown in Fig. 6a–d. We analyzed the light intensities in an arbitrary unit of the mCherry labelled cell bodies (in red dots) within and outside of the transparent microelectrode area. The transmittance rate of the transparent microelectrodes was derived by comparing the maximum light intensities of selected labelled cell bodies *via* Matlab to eliminate the interference of 10 μm parylene C. The calculated transmittance rate of the transparent microelectrode area was above 95.7%, indicating the excellent fluorescent transparency of our PEDOT–ITO–Ag–ITO thin films. Also of note is the shadowing effect of the top parylene C encapsulation over the electrode edge and trace areas under the bright field condition (Fig. 6b), due to extra absorption and reflection at the top parylene–ITO interface. This top encapsulation does not impact the transparency of the array under fluorescent imaging, as indicated in Fig. 6a.

In vivo acute animal experiments were conducted to evaluate the surgical and functionality of the devices on V1 of rats. During the *in vivo* experiments, the developed μECoG array was gently placed on both the left and right lobes of V1 (Fig. S5†). The left V1 was stimulated with the light stimuli under high or low intensity, while the right V1 served as a control. Light-evoked ECoG activities were recorded from both V1 lobes *via* the implanted microelectrodes, and the neural recordings were analyzed over a time span of 20 s and compared with a baseline that was recorded when the LED stimulation was turned off. Fig. 6e show that the ECoG activity evoked by the high-intensity stimulus had significantly larger energy variations compared to both the baseline and activity evoked by the low-intensity stimulus. Furthermore, Hilbert transformation was applied to extract the instantaneous phases of 150 trails of ECoG recordings

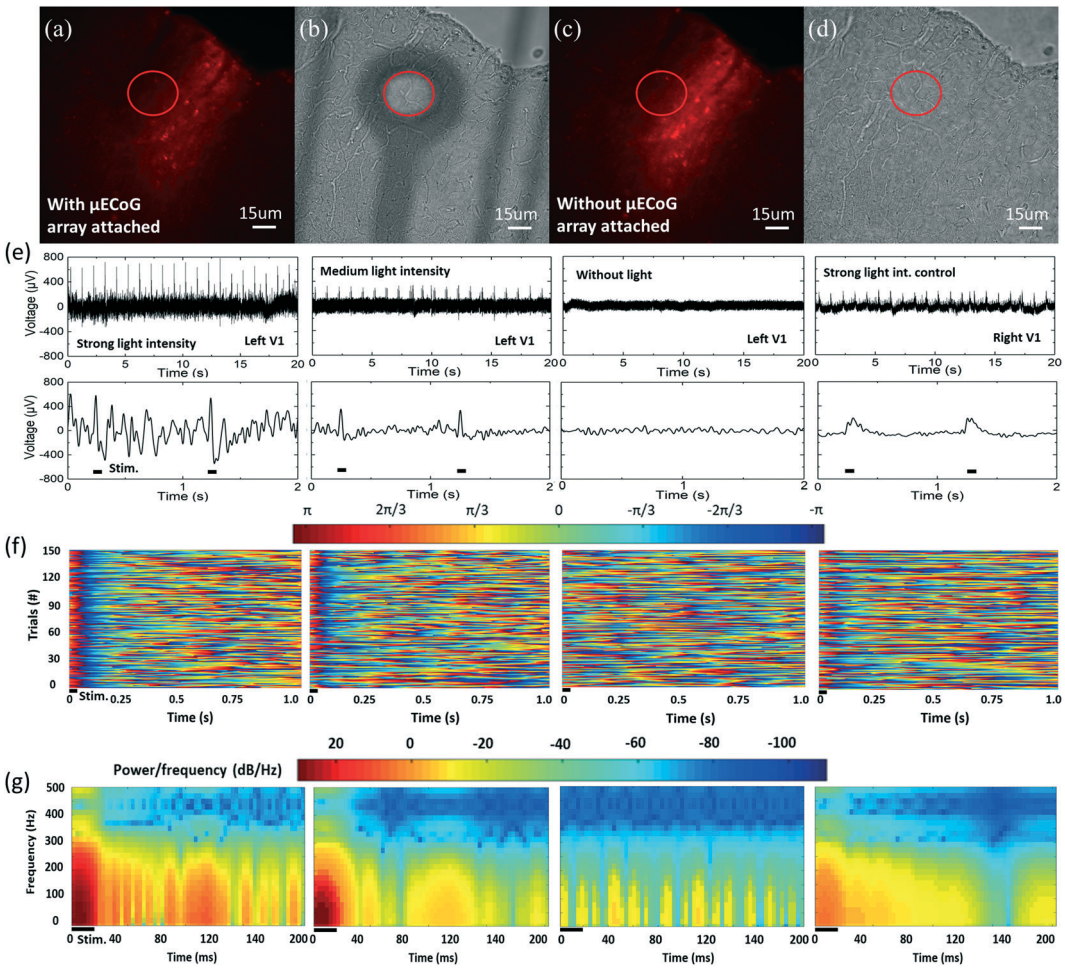

Fig. 6 Fluorescent and bright-field images of mCherry-labelled rat brain section and *in vivo* recording results of light-evoked field potentials. Leica mCherry fluorescent images a and c and bright-field images b and d with and without the transparent μECoG array attached on. *In vivo* test data of e signal amplitudes, f instantaneous phases, and g PSD spectrograms of left and right V1 with the strong light stimulations, medium light stimulations, and without visual stimulation.

within a frequency range of 1–25 Hz. As shown in Fig. 6f, the 150 trails are aligned to the concurrence of the stimulus and stacked, and the colors indicate the instantaneous phase of each trail. The baseline and control did not show significant phase synchrony, while strong and reliable phase-locked synchronization was observed across 150 trials of signals recorded with the high light stimulation. The instantaneous phase that resulted from the low-intensity stimulation showed only slight synchronization, as expected. Additionally, 150 trial ECoG recordings were averaged and mapped onto a time-frequency graph of color-coded, normalized power spectral density (PSD) distribution (Fig. 6g). A significant increase of PSD was observed in a short time window of ~200 ms following the light stimulation compared to the control baseline. Higher light intensity resulted in higher PSD compared to that seen with lower optical stimulation.[46] The control also showed increased PSD at the onset of high-intensity stimulation, which may have been caused by the electrical artifacts of the LED. These results suggest that the optical stimulation can effectively evoke neural activity and that our transparent microelectrode array can successfully record light-evoked ECoG oscillations.

Conclusions and discussion

In summary, we have demonstrated a conductive, anti-reflective, transparent and ultra-flexible μECoG array using PEDOT:PSS–ITO–Ag–ITO multilayer thin films on parylene C. This PEDOT:PSS–ITO–Ag–ITO based μECoG array exhibits significantly reduced sheet resistance, remarkable transmittance, good electrochemical impedance, increased charge storage capacity, excellent SNRs, and the capacity for *in vivo* ECoG recordings. The effects of sputtering temperature and film thickness on the performance of the combined assemblies were fully studied to optimize the creation of combined thin films with the desired properties. The tunable peak transmittance was confirmed with different film combinations designed using the theoretical admittance loci optimization under selected wavelengths of 470 nm, 550 nm, and 630 nm. The optimized multilayer PEDOT:PSS–ITO–Ag–ITO film was fully characterized using various experimental methods. Particularly, the EIS and CV analyses demonstrated the significantly enhanced electrical impedance of the PEDOT:PSS–ITO–Ag–ITO film (by 91.85%). We compared other recently reported transparent ECoG arrays with ours and make a benchmark table, as shown in Table 2.

The combined thin films remained stable over 12 weeks in both air and saline environments at 37 °C, confirming their long-term stability. Meanwhile, peel-off tests verified the excellent adhesion of the ITO–Ag–ITO assembly on the parylene C substrate, and bending test results demonstrated the mechanical flexibility of combined thin films. The slight increase in the film sheet resistance during the bending test was believed to be mainly caused by cracks under repetitive mechanical stressing. Future studies would be focused on identifying the failure modes using analytical tools such as scanning electron microscopy (SEM) as well as testing the bending performance of the ITO–Ag–ITO interconnects sandwiched between two parylene C layers. We will also modify the experimental protocols to enable continuous measurement of the changes in the trace resistance during bending as an indication of the failure.

The Young's modulus of the combined film was tested to be ~4 GPa, dominated by the parylene C substrate. The flexibility of the combined film could be further improved by switching parylene C to another polymeric material with a lower Young's modulus, such as PDMS. Moreover, SNRs were measured under various color LEDs, confirming the negligible photon-induced artifacts of recordings using the combined film. The optical transmittance of the transparent microelectrode array was further demonstrated under both fluorescent and bright-field illumination conditions. Finally, *in vivo* animal experiments validated the ability to use these transparent microelectrodes to record optogenetically evoked ECoG activity from the rat visual cortex.

It is worth noting that the parylene C insulation greatly reduced the transparency of the μECoG device, particularly in the shorter wavelength range (*i.e.* blue light), due to the absorptive and reflective loss in parylene layers. Future studies could fruitfully explore this issue by further analyzing and refining the dimension design of each layer to make the whole μECoG device more transparent over a broad spectrum. In addition, fabricating anti-reflective moth-eye nanostructure at the backside of parylene C could be considered to further improve the transmittance of ECoG arrays,[50] as well as perform a better antibacterial effect.[51] Instead of increasing deposition temperature, the quality of the room temperature ITO could be improved with other

Table 2 Benchmark table of transparent ECoG arrays

Materials	Transmission	1 K kHz impedance (Ω cm^2)	Ref.
Silver nanowires + indium-doped zinc oxide (IZO)	~73.8%	~45.16	47
Gold nanonetwork	87%	~18.60	48
ITO	>80%	~65.21	16
PEDOT:PSS–graphene	<50%	~0.21–~0.3	42, 43
Carbon nanotube	>85%	~20	49
Graphene	>90%	~22.49	22
Gold nanomesh	>70%	~8.14	17
PEDOT:PSS–ITO–Ag–ITO	89%	~0.81	Our work

methods, such as ion source assisted sputtering,[52] which not only improves the electrical and optical properties of the ITO film but also enhances the film stability due to increased density with fewer pinholes (Fig. S6†). An alternative approach to improve the ITO film quality is low-temperature plasma annealing,[29] which has been proved to enable relatively low resistivity (2.5×10^{-3} Ω cm) and high optical transmission (94%) while allowing multiple wafer processing in parallel.

Materials and methods

ITO film deposition

To study temperature effect, 100 nm ITO films were sputtered with RF magnetron sputtering system on glass or parylene-coated glass substrates. Before the ITO sputtering, glass slides were ultrasonically cleaned in an acetone bath to remove organic contaminants and particles, followed by rinses with ethanol, isopropanol, and deionized (DI) water. Then, the glass slides were dried in a N_2 stream and baked on a hotplate at 100 °C for 30 min. For some samples, 10 μm parylene C was deposited on the cleaned glass slides using chemical vapor deposition (PDS 2010, Specialty Coating System, Inc). The sputtering process was conducted in an RF magnetron sputtering system (Denton Explorer-14, Denton Vacuum, Inc) using a 4 inch diameter ITO target (99.99% purity) which contains 90% indium oxide and 10% tin oxide. The heater was turned on when the turbo pump was on to provide sufficient time for the substrate temperature to increase to the setup value. After the base pressure inside the chamber was decreased below 2×10^{-6} Torr, 60 sccm argon was introduced into the deposition chamber to achieve 3×10^{-3} Torr sputtering pressure. Substrate rotating speed was set up at 20% to ensure the sputtering uniformity. Ten min pre-sputtering was performed to remove the contaminants on the target surface. During the deposition, the sputtering RF power was set up at 100 watts with a deposition rate of 1.064 Å s^{-1}. After the sputtering, the heater was turned off immediately and the samples were taken out after the chamber was cooled down to room temperature.

Fabrication of PEDOT:PSS–ITO–Ag–ITO thin films

The following fabrication steps are illustrated based on the PEDOT:PSS (30.5 nm)–ITO (24 nm)–Ag (9.45 nm)–ITO (20 nm) assembly designed under 550 nm wavelength. The ITO layers were sputtered with the same steps described above. For Ag deposition, a 4 inch diameter Ag target (99.99% purity) was installed as another cathode in the Denton system. The base pressure, sputtering pressure, and sputtering RF power were kept the same as the ITO sputtering procedure, which results in a deposition rate of 4.318 Å s^{-1}. The substrate rotating speed was increased to 70%. ITO–Ag–ITO deposition was finished layer by layer consecutively without breaking the chamber vacuum. To add the PEDOT:PSS coating, 0.55% PEDOT:PSS solution, which was diluted from 1.1% PEDOT:PSS (768642, Sigma-Aldrich), was spun on top of the as-deposited ITO–Ag–ITO substrate with 500 rpm, 5 s ramping followed by full spin at 4000 rpm for 120 s. The PEDOT:PSS coating was then dehydrated on a hotplate at 100 °C for 30 min.

Fabrication of μECoG array

First, 10 μm parylene C was deposited on a cleaned 3 inch silicon wafer. Then, a photoresist (PR) layer was spun on the substrate and photolithographically patterned to expose the areas of microelectrodes, interconnection wires, and contact pads. Following ITO–Ag–ITO deposition using the above method, the wafer was submersed in acetone at room temperature. With the PR mask, ITO–Ag–ITO on the undesired areas was washed off with acetone and the surface was cleaned with isopropyl alcohol (IPA) and deionized (DI) water, leaving the ITO–Ag–ITO on the electrode sites, contact pads, and interconnect wires. Next, 2 μm parylene C was deposited on the substrate as an insulating layer, and then parylene C on the contact pads and microelectrodes were removed completely using oxygen plasma dry etching (RIE-1701 plasma system, Nordson March, Inc). Then, 500 nm copper was sputtered and patterned only on the contact pad with a sacrificial PR mask. Then, PR was rinsed off with acetone, IPA and DI water for copper lift off. After that, another PR mask was patterned to expose only the microelectrode sites followed by spin coating of diluted 0.55% PEDOT:PSS using the above recipe. Finally, PR was rinsed off with acetone, IPA and DI water to remove unwanted PEDOT:PSS, leaving PEDOT:PSS only on top of the ITO–Ag–ITO microelectrodes. Instead of using plasma etching, the outer shape of the array was manually cut according to the defined outlines that we initially designed on our mask to prevent the damage of ITO from plasma over-etching. The detailed fabrication steps are shown in Fig. S7.†

TEM samples preparation and test

Samples were prepared by sputtering ITO thin films on TEM carbon grid holders using the aforementioned deposition procedures. Then carbon grid samples were loaded and tested individually in the TEM (JEOL 2200FS, JEOL, Inc) for imaging and X-ray diffraction analysis.

Transmittance and conductivity measurements

Filmetrics thin film analyzer was utilized to measure the transmittance of thin films in air over a wavelength range of 300–800 nm (F20-UVX, Filmetrics, Inc) and four-point probe (SRM-232, Bridge Technology, Inc) was applied to measure the sheet resistances of the samples. The mCherry fluorescent images and bright-field were taken by a THUNDER imager (3D Cell Culture, Leica, Inc).

Electrochemical measurements

Electrochemical impedance spectrometry (EIS) measurements were performed using a potentiostat (Electrochemical

Analyzer, CH Instruments, Inc.) to analyze the electrochemical impedance in a three-electrode cell, with the microelectrode as the working electrode (WE), an Ag/AgCl electrode as the reference electrode (RE), and a platinum electrode as the counter electrode (CE). The tests were conducted in the physiological saline solution (0.9% NaCl) at room temperature. The electrochemical impedance of the microelectrode was measured from 0.1 Hz to 100 kHz when a 5 mV RMS sinusoid waveform was applied to the WE. Cyclic voltammograms (CVs) of the microelectrode were measured at a 100 mV s^{-1} sweep rate in a potential range of −0.9 V to 0.9 V. Multiple CV scans were done in experiments before data collection to clean the electrode surface and allow the system to settle.

Peel-off tests

5 samples for peel-off tests were prepared by sputtering 100 nm ITO directly on 10 μm parylene C coated glass slides following by blade cutting to divide the entire film to a 10 × 10 array of 1 mm^2 squares. The cut was carefully made only through the 100 nm ITO layer without damaging the parylene C substrate. The success of blade-cutting was confirmed *via* a digital multimeter (Fluke-115, Fluke, Inc). Scotch tape test was processed by applying Scotch No. 810 pressure-type tape on the ITO–parylene C samples for 50 repetitive cycles with 180° peel-off angle. After each peel off, the samples were inspected visually under a microscope to track whether there was any ITO delamination from the parylene C substrate.

Bending tests and Young's modulus measurements

The bending tests were conducted under bending curvatures of 3 mm and 6 mm in diameter, respectively. The sheet resistances of the combined films with different ITO thicknesses were measured every 100 bending cycles for a total of 1000 cycles. The Young's moduli of the combined films on parylene C and the single layer of parylene C were measured using the MTS Nanoindenter XP system (Nano Indenter XP, MTS System, Inc), and the experimental values were compared with the theoretical values.

Signal to noise ratios (SNRs) measurements

The microelectrode array and LEDs of different colors were immersed in the saline solution with a separation distance of ~0.5 cm. A 1 mV_{pp} sinusoidal waveform at 5 Hz frequency was applied at the opposite ends of the saline solution container. LEDs were kept flashing on the microelectrode panels with applied voltages of V_{blue} = 3.3 V, V_{green} = 3.3 V, V_{yellow} = 1.8 V, and V_{red} = 1.8 V, respectively. The whole setup was placed in a Faraday cage to minimize the environmental noises. The signals were acquired *via* an RHD2132 system (Intan Technologies, Inc), and then analyzed with OriginLab and Excel to calculate the SNRs.

In vivo animal experiment

One male adult rat (Sprague Dawley, 435 g) was tested based on our established protocols approved by the Institutional Animal Care and Use Committee (IACUC) at Michigan State University. Following the stereotaxic surgery protocol, an adeno-associated virus (AAV) vector containing the channel rhodopsin and mCherry genes (AAV-hSyn-hChR2 (H134R)-mCherry; UNC Vector Core) was injected bilaterally into the rat's V1. After injection, the rats were kept in the animal facility for 4 weeks until the V1 neurons expressed channelrhodopsin-2 (ChR2). During the *in vivo* experiments, the rat was anesthetized with 2% isoflurane and oxygen (0.8 L min^{-1}) and placed in a stereotaxic apparatus. Using sterile surgical procedures, a 3–4 cm incision was made in the skin overlying the skull and a small region of bone was removed to expose the V1 areas. The μECoG array was carefully attached to the V1 region using a micromanipulator. A wireless-powered micro-LED was placed over the μECoG array on the left V1 area, with a light pulse duration of 20 ms at 1 Hz frequency and with 1.5 mW mm^{-2} low light intensity or 11.8 mW mm^{-2} high light intensity. The microelectrodes on the left panel were illuminated directly by the micro-LED. Light-evoked ECoG activity was simultaneously recorded through the implanted microelectrodes. Spontaneous ECoG activities recorded from the left V1 when LED light was completely off were used as a positive control, while a negative control consists of ECoG recordings from the right V1 when the left V1 underwent high optical stimulation. The recorded signals were amplified and digitalized using a commercial Intan RHD2132 system (Intan Technologies) and then analyzed using the Matlab Chronux toolbox to extract the activation energy, phase synchrony, PSD distribution from the recordings.

Author contributions

W. Y., Q. H. F., and W. L. proposed the idea of this project. W. Y. and M. S. ran the depositions. W. Y. performed all the microfabrication and characterization experiments. W. Y., Y. G., Y. J., A. W., and W. L. performed the *in vivo* animal experiments. W. Y., C. Y., and Z. Q. took the fluorescent images. W. Y. and W. L. wrote the manuscript. A. W. and Q. H. F. reviewed the manuscript.

Conflicts of interest

There are no conflicts to declare.

Acknowledgements

This work was supported through the National Science Foundation under the Award Number ECCS-1923187 and CMMI-1724941, and Michigan State University.

References

1 V. L. Feigin, E. Nichols, T. Alam, M. S. Bannick, E. Beghi, N. Blake, W. J. Culpepper, E. R. Dorsey, A. Elbaz and R. G. Ellenbogen, *Lancet Neurol.*, 2019, **18**, 459–480.

2 F. Seifar, M. Khalili, H. Khaledyan, S. Amiri Moghadam, A. Izadi, A. Azimi and S. K. Shakouri, *Nutr. Neurosci.*, 2019, **22**, 306–316.
3 M. M. Kurtis, T. Rajah, L. F. Delgado and H. S. Dafsari, *npj Parkinson's Dis.*, 2017, **3**, 1–12.
4 K. D. Wise, J. B. Angell and A. Starr, *IEEE Trans. Biomed. Eng.*, 1970, 238–247.
5 X. Xu, T. Mee and X. Jia, *Crit. Rev. Biochem. Mol. Biol.*, 2020, **55**, 1–16.
6 E. Montagni, F. Resta, A. L. A. Mascaro and F. S. Pavone, in *Photonics*, Multidisciplinary Digital Publishing Institute, 2019, vol. 6, p. 92.
7 W. Yang, W. Khan, J. Wu and W. Li, *J. Micromech. Microeng.*, 2019, **29**, 43001.
8 E. Montagni, F. Resta, A. L. A. Mascaro and F. S. Pavone, in *Photonics*, Multidisciplinary Digital Publishing Institute, 2019, vol. 6, p. 92.
9 B. Ji, C. Ge, Z. Guo, L. Wang, M. Wang, Z. Xie, Y. Xu, H. Li, B. Yang and X. Wang, *Biosens. Bioelectron.*, 2020, 112009.
10 W. Yang, A. Broski, J. Wu, Q. H. Fan and W. Li, *IEEE Trans. Nanotechnol.*, 2017, **17**, 701–704.
11 D. Khodagholy, J. N. Gelinas, T. Thesen, W. Doyle, O. Devinsky, G. G. Malliaras and G. Buzsáki, *Nat. Neurosci.*, 2015, **18**, 310–315.
12 N. M. Ahmed, F. A. Sabah, H. I. Abdulgafour, A. Alsadig, A. Sulieman and M. Alkhoaryef, *Results Phys.*, 2019, **13**, 102159.
13 J.-B. Lyau, H.-C. Wu and H. Chen, in *Tin Oxide Materials*, Elsevier, 2020, pp. 599–613.
14 S. Ziaei, Q. Wu, J. Fitch, M. Elbadry and M. A. Zikry, *Exp. Mech.*, 2019, **59**, 703–712.
15 A. Zátonyi, M. Madarász, Á. Szabó, T. Lőrincz, R. Hodován, B. Rózsa and Z. Fekete, *J. Neural Eng.*, 2020, **17**, 16062.
16 Y. Bi, Y. Liu, X. Zhang, D. Yin, W. Wang, J. Feng and H. Sun, *Adv. Opt. Mater.*, 2019, **7**, 1800778.
17 K. J. Seo, Y. Qiang, I. Bilgin, S. Kar, C. Vinegoni, R. Weissleder and H. Fang, *ACS Nano*, 2017, **11**, 4365–4372.
18 Z. Chen, R. T. Yin, S. N. Obaid, J. Tian, S. W. Chen, A. N. Miniovich, N. Boyajian, I. R. Efimov and L. Lu, *Adv. Mater. Technol.*, 2020, 2000322.
19 Y. Qiang, P. Artoni, K. J. Seo, S. Culaclii, V. Hogan, X. Zhao, Y. Zhong, X. Han, P.-M. Wang and Y.-K. Lo, *Sci. Adv.*, 2018, **4**, eaat0626.
20 Y. Qiang, K. J. Seo, X. Zhao, P. Artoni, N. H. Golshan, S. Culaclii, P. Wang, W. Liu, K. S. Ziemer and M. Fagiolini, *Adv. Funct. Mater.*, 2017, **27**, 1704117.
21 K. J. Seo, P. Artoni, Y. Qiang, Y. Zhong, X. Han, Z. Shi, W. Yao, M. Fagiolini and H. Fang, *Adv. Biosyst.*, 2019, **3**, 1800276.
22 D.-W. Park, J. P. Ness, S. K. Brodnick, C. Esquibel, J. Novello, F. Atry, D.-H. Baek, H. Kim, J. Bong and K. I. Swanson, *ACS Nano*, 2018, **12**, 148–157.
23 D.-W. Park, S. K. Brodnick, J. P. Ness, F. Atry, L. Krugner-Higby, A. Sandberg, S. Mikael, T. J. Richner, J. Novello and H. Kim, *Nat. Protoc.*, 2016, **11**, 2201.
24 D.-W. Park, A. A. Schendel, S. Mikael, S. K. Brodnick, T. J. Richner, J. P. Ness, M. R. Hayat, F. Atry, S. T. Frye and R. Pashaie, *Nat. Commun.*, 2014, **5**, 5258.
25 L. V. Kayser and D. J. Lipomi, *Adv. Mater.*, 2019, **31**, 1806133.
26 C. C. Lee, D. L. Wang, C. C. Chen, J. Y. Chang, B. J. Pong, G. C. Chi and L.-W. Wu, in *Sixth International Conference on Solid State Lighting*, International Society for Optics and Photonics, 2006, vol. 6337, p. 63370E.
27 H. A. Macleod, *Thin-film optical filters*, CRC press, 2017.
28 E. Klein, K. Huber, O. Paul and P. Ruther, *Thin Solid Films*, 2020, **693**, 137715.
29 H. Ohsaki, M. Suzuki, Y. Shibayama, A. Kinbara and T. Watanabe, *J. Vac. Sci. Technol., A*, 2007, **25**, 1052–1055.
30 W. Chung, M. O. Thompson, P. Wickboldt, D. Toet and P. G. Carey, *Thin Solid Films*, 2004, **460**, 291–294.
31 S. Ishibashi, Y. Higuchi, Y. Ota and K. Nakamura, *J. Vac. Sci. Technol., A*, 1990, **8**, 1403–1406.
32 C.-W. Lin, K.-P. Chen, M.-C. Su, T.-C. Hsiao, S.-S. Lee, S. Lin, X. Shi and C.-K. Lee, *Sens. Actuators, B*, 2006, **117**, 219–229.
33 Y.-J. Jen, W.-C. Liu, T.-K. Chen, S. Lin and Y.-C. Jhang, *Sci. Rep.*, 2017, **7**, 1–10.
34 E. A. Pama, L. S. Colzato and B. Hommel, *Front. Psychol.*, 2013, **4**, 610.
35 I. Nuramdhani, A. T. Gokceoren, S. A. Odhiambo, G. De Mey, C. Hertleer and L. Van Langenhove, *Materials*, 2018, **11**, 48.
36 V. Radun, R. P. von Metzen, T. Stieglitz, V. Bucher and A. Stett, *Curr. Dir. Biomed. Eng.*, 2015, **1**, 493–497.
37 C. A. Schuh, *Mater. Today*, 2006, **9**, 32–40.
38 Y. Sun, R. P. Padbury, H. I. Akyildiz, M. P. Goertz, J. A. Palmer and J. S. Jur, *Chem. Vap. Deposition*, 2013, **19**, 134–141.
39 F. Ejserholm, J. Stegmayr, P. Bauer, F. Johansson, L. Wallman, M. Bengtsson and S. Oredsson, *Biomater. Res.*, 2015, **19**, 19.
40 T. Wittkowski, J. Jorzick, H. Seitz, B. Schröder, K. Jung and B. Hillebrands, *Thin Solid Films*, 2001, **398**, 465–470.
41 L. D. Garma, L. M. Ferrari, P. Scognamiglio, F. Greco and F. Santoro, *Lab Chip*, 2019, **19**, 3776–3786.
42 J. Park, F. Sun, Y. Xie, Z. Xiong and G. Xu, *IEEE Electron Device Lett.*, 2020, **41**, 1261–1264.
43 P. Kshirsagar, S. Dickreuter, M. Mierzejewski, C. J. Burkhardt, T. Chassé, M. Fleischer and P. D. Jones, *Adv. Mater. Technol.*, 2019, **4**, 1800318.
44 M. P. De Jong, L. J. Van Ijzendoorn and M. J. A. De Voigt, *Appl. Phys. Lett.*, 2000, **77**, 2255–2257.
45 W. Yang, J. Wu, Q. H. Fan and W. Li, in *2019 IEEE 32nd International Conference on Micro Electro Mechanical Systems (MEMS)*, IEEE, 2019, pp. 525–528.
46 M. Le Van Quyen, J. Foucher, J.-P. Lachaux, E. Rodriguez, A. Lutz, J. Martinerie, F. J. Varela and J. Neurosci, *Methods*, 2001, **111**, 83–98.
47 J. P. Neto, A. Costa, J. V. Pinto, A. Marques-Smith, J. Costa, R. Martins, E. Fortunato, A. R. Kampff and P. Barquinha, bioRxiv.
48 J. Seo, K. Kim, K. Seo, M. K. Kim, S. Jeong, H. Kim, J. Ghim, J. H. Lee, N. Choi and J. Lee, *Adv. Funct. Mater.*, 2020, **30**, 2000896.

49 J. Zhang, X. Liu, W. Xu, W. Luo, M. Li, F. Chu, L. Xu, A. Cao, J. Guan and S. Tang, *Nano Lett.*, 2018, **18**, 2903–2911.
50 C. Zhang, Y. Zhu, P. Yi, L. Peng and X. Lai, *J. Micromech. Microeng.*, 2017, **27**, 75010.
51 K. Minoura, M. Yamada, T. Mizoguchi, T. Kaneko, K. Nishiyama, M. Ozminskyj, T. Koshizuka, I. Wada and T. Suzutani, *PLoS One*, 2017, **12**(9), e0185366.
52 M. S. Farhan, E. Zalnezhad, A. R. Bushroa and A. A. D. Sarhan, *Int. J. Precis. Eng. Manuf.*, 2013, **14**, 1465–1469.